

Research Article

Determination of Geometric Parameters of Cracks in Concrete by Image Processing

Yuriy Vashpanov ¹, Jung-Young Son,² Gwanghee Heo ¹, Tatyana Podousova,³
and Yong Suk Kim⁴

¹Civil Engineering Department, Public Safety Research Institute, Konyang University, Nonsan, Chungnam 32992, Republic of Korea

²Biomedical Engineering Department, Public Safety Research Institute, Konyang University, Nonsan, Chungnam 32992, Republic of Korea

³Applied Mathematics Department, Odessa State Academy of Civil Engineering and Architecture, Odessa 65029, Ukraine

⁴Bio-IT Engineering Department, Public Safety Research Institute, Konyang University, Nonsan, Chungnam 32992, Republic of Korea

Correspondence should be addressed to Yuriy Vashpanov; yuriy.vashpanov@gmail.com

Received 31 May 2019; Revised 7 August 2019; Accepted 24 September 2019; Published 30 October 2019

Academic Editor: Mohamed ElGawady

Copyright © 2019 Yuriy Vashpanov et al. This is an open access article distributed under the Creative Commons Attribution License, which permits unrestricted use, distribution, and reproduction in any medium, provided the original work is properly cited.

The 8-bit RGB image of a cracked concrete surface, obtained with a high-resolution camera based on a close-distance photographing and using an optical microscope, is used to estimate the geometrical parameters of the crack. The parameters such as the crack's width, depth, and morphology can be determined by the pixel intensity distribution of the image. For the estimation, the image is transformed into 16-bit gray scale to enhance the geometrical parameters of the crack and then a mathematical relationship relating the intensity distribution with the depth and width is derived based on the enhanced image. This relationship enables to estimate the width and depth with $\pm 10\%$ and $\pm 15\%$ accuracy, respectively, for the crack samples used for the experiments. It is expected that the accuracy can be further improved if the 8-bit RGB image is synthesized by the images of the cracks obtained with different illumination directions.

1. Introduction

Cracks in concretes are one of the important parameters in diagnosing the current status of structures [1–3]. The changing sizes and depths of the cracks in time are a barometer of predicting the safety of a structure. Hence, the demands of measuring the geometrical parameters of the cracks accurately are ever increasing [4–8], and the number of articles for crack measurements has also been increased [9–17]. In this process, many methods such as using ultrasounds [18–21], X-rays [22], and eddy current (EC) [23] sources are developed, and the images are reconstructed in 3D (three-dimensional) [24] form. Hence, it is considered that these methods have good prospects for practical use in civil engineering [25]. But, these methods require that the

sources should be contacted to the concrete surface tightly to deliver the source energy to the concrete without much loss. They require specialists and are inconvenient to use and time consuming. The more convenient and less time-consuming method is using a camera to take the image of the cracked concrete surface. Since it is a noncontact method of detecting the cracks and requires no specialist, the camera can be even mounted on a drone to cover a bridge. In the photos, the cracks are easily identified because of their darkness in comparison with the concrete surface. Software and hardware tools can easily determine the width and length of the cracks with sufficient accuracy from the image in each photo [17, 26–28]. Added on this, the photographing distances can be varied significantly with use of a telephoto lens [29]. Hence, the camera method is very convenient to

use in the places like difficult to access. But, it also has a problem because the crack depth which informs the amount of crack penetration and of crack propagation direction inside the structures can be hardly estimated. Due to the fact that the cracks in the photo appear as lines, they do not have enough pixels to process to extract their depth information.

Since the image from a color digital camera consists of a number of pixels corresponding to the camera resolution and each pixel consists of R (red), G (green), and B (blue) subpixels for the color presentation, the pixel color is determined by the relative intensity ratio of the RGB colors in the light coming into the pixel. The pixel intensity is represented as 8-bit gray level; i.e., there are 256 intensity levels depending on the light amount. Since each pixel in the image has a corresponding crack or concrete surface point, the light amount coming into each pixel is related to the point distance from the illuminating light source and the camera because the light intensity is reduced in proportional to the distance square. This is why the cracks appear as darker than the surface because they have longer distances than the surface. Since the intensity of each pixel has the distance information of its corresponding object point, the depth of the crack can be estimated by setting each of the camera and the illumination source to a fixed distance from the concrete surface containing the crack. Hence, measuring the pixel intensity distribution of the crack image will provide simultaneously the crack width, depth, and shape information. In this case, the camera needs to have a high resolution and be located at a close distance from the crack to have more pixels on its portion for the better accuracy. More pixel numbers make the intensity distribution describe more clearly and accurately the shape, depth, and width of the crack. Transforming the pixel intensity level to 16 bits' grey level from the 8 bits as in the OriginLab [30] will enhance the depth resolution of the crack depth. The first approach of estimating the crack depth with use of a camera image was finding the average pixel intensity value of the crack area in the image [31]. But, this pixel intensity is only for the crack depth but not for width and shape of the crack.

In this paper, the pixel intensity distribution of crack images that are obtained with a high-resolution camera at a close distance to the crack is used to estimate the crack's width, depth, and shape. The distribution allows estimating the crack's depth and shape size that cannot be possible with the typical camera images of cracks.

2. Experimental Setup for Obtaining Images of Cracks in Samples

Obtaining high-quality images of cracks depend on camera resolution, properties of objective, and photographing parameters (the distance to the object, the illumination parameters of the light source, and the camera depth of field). Since the size of cracks can also be different from tens of millimeters to tens of microns, the photographing setup should be different for different crack sizes. For this reason, two experimental setups are used, as shown in Figure 1(a): one is using a close distance camera to the crack and the other is a microscope. The 1st setup consists of a high-

resolution Nikon D810 camera (2) for photographing, and a halogen lamp (4) for illuminating an experimental sample (1) having a crack on its surface. The 2nd setup consists of a binocular microscope (5) for magnifying the crack image, a Raspberry Pi camera v2 (3) installed at one eye position of the microscope for recording the image, and the halogen lamp (4), the same as in the 1st setup. These optical setups are on an optical table (9), and the Raspberry Pi camera is connected to a monitor (8) to check the crack image. The Nikon camera has the maximum resolution of 7360×4912 pixels with a pixel size of $4.88 \mu\text{m} \times 4.88 \mu\text{m}$ [32]. The Raspberry Pi camera has the resolution of 3280×2464 pixels with a pixel size of $1.12 \mu\text{m} \times 1.12 \mu\text{m}$ [33]. The halogen lamps can illuminate the experimental sample surface at an angle of about 30 degrees to the normal direction of the optical table. The illuminance of the experimental sample from a halogen lamp is around 57 klx for the 1st setup and around 110 klx for the 2nd setup. This illuminance is measured with a T10 illuminance meter from Konica Minolta Sensing Inc. [34]. In the setups, the positions of the lamps and the cameras were strictly fixed and the amounts of lights from the lamps are constant. To match the sample to the camera and the lamp positions, the sample is mounted on a combined stage (6) of a microtranslator and 360° rotator for precisely shifting and rotating the sample to a required position and to any angle with the accuracy of 1° , respectively. The stage is also mounted on a height control stage (7) for the precise adjustment of the sample position. The experimental samples are the jaws of a caliper, a cracked concrete block on its surface having the size of 5 cm (width) \times 5 cm (height) \times 20 cm (length), heat dissipater with multiple blades, and a brick wall of a building. Figure 1(b) shows the equivalent optical photographing geometry of Figure 1(a). It can be applicable to both experimental setups. The camera and microscope objectives are represented as a lens and the camera's image detector as the plane containing x_i and y_i which represent the width and length of the crack image, respectively. The crack and the experimental sample surface are represented as the dent and the side wings, respectively, in the bottom shape. In Figure 1(b), L is the distance between the lens and the experimental sample surface, d crack depth, f the focal length of the lens, and x and y width and length of the crack, respectively. From Figure 1(a), a relationship between these symbols can be derived: according to the similar triangle relationship,

$x_i/x = l/L$ and $y_i/y = l/L$. In these relationships, l and L are related as $l/l + 1/L = 1/f$ [35] by the Gaussian lens formula; by combining them, the width x and length y of the crack can be rewritten as

$$\begin{aligned} x &= x_i \frac{L-f}{f} = n_1 \delta \left(\frac{L}{f} - 1 \right) = n_1 \delta (\zeta - 1), \\ y &= y_i \frac{L-f}{f} = n_2 \delta \left(\frac{L}{f} - 1 \right) = n_2 \delta (\zeta - 1), \end{aligned} \quad (1)$$

where $\zeta = L/f$, $x_i = n_1 \delta$, and $y_i = n_2 \delta$, δ is a pixel size, and n_1 and n_2 are the pixel numbers corresponding to the crack width and length on image. The geometrical crack sizes can

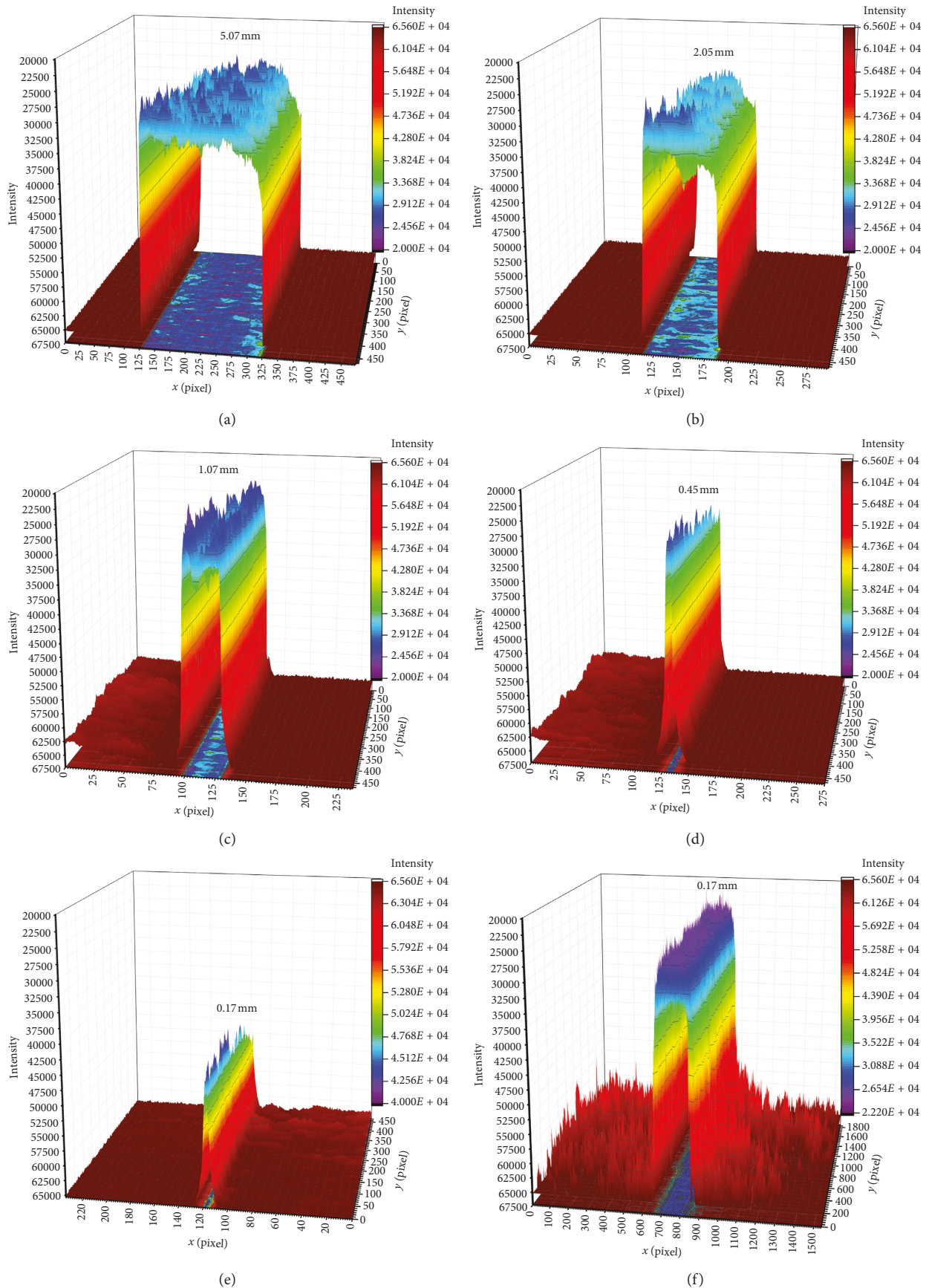


FIGURE 3: 3D plotting of the intensity distributions corresponding to the caliper's gap sizes of (a) 5.07 mm, (b) 2.05 mm, (c) 1.07 mm, (d) 0.45 mm, (e) 0.17 mm, and (f) 0.17 mm with the microscope.

can transform the original 8-bit RGB color image into an 8 or 16-bit, i.e., a 65,536 gray-level image, and then convert the image to an intensity matrix. So, any image can be represented in the form of an intensity matrix having the dimension of the image's pixel resolution. Each element of the matrix represents the light intensity of its corresponding pixel of the crack image. The light intensity value in the OriginLab is represented as a color scale to enhance the perception of intensity gradations compared to the original image.

For the 1st experimental sample, the gap between the jaws of a Mitutoyo caliper is used because the geometrical parameters of the gap are known with a high accuracy. The gap width can be adjusted from 0 to 4 inch with the resolution of 0.0005 inch, and the jaws have a thickness of 3.50 ± 0.03 mm [37]. The thickness of the jaws is considered as the crack depth. The gap between jaws is set to five different values of 5.07 mm, 2.05 mm, 1.07 mm, 0.45 mm, and 0.17 mm to compare the resolutions of two experimental setups, as shown in Figure 2. Figure 2 shows the sizes of the five different gaps between two jaws of the caliper. The gaps will work as the widths of the cracks. The caliper is on a thick flat paper with a dark surface. The paper works as the bottom of the cracks. Hence, the gaps between the jaws will work like rectangular parallelepiped shape cracks. These cracks have the same depth and length but different widths as specified above. Figure 3 shows a 3D plotting of the pixel intensity distributions processed by OriginLab with the camera images of two setups. x and y axes represent the pixel coordinate and z -axis intensity. The lowest intensity level of the z -axis is the same for all figures. Figures 3(a)–3(f) are for 5.07 mm, 2.05 mm, 1.07 mm, 0.45 mm, 0.17 mm, and 0.17 mm with the microscope, respectively. The 1st five distributions are from the images with the 1st experimental setup. Figures 3(a)–3(c) inform that (1) the morphologies of the 3D intensity distributions for the first 3 gaps are having near rectangular parallelepiped shapes, (2) their intensity differences between the low- and high-intensity distributions are nearly the same as 3.2×10^4 , (3) the top edges of the distributions have a circular shape, especially for Figures 3(a) and 3(b), and (4) almost no intensity peaks are appearing in the dark red part regions but many intensity peaks in blue and sky blue regions. (1) and (2) indicate that the intensity distribution can correctly describe the crack shape and depth. However, (3) and (4) inform the presence of error in the shape and the depth. The intensity peaks in the figures and the circular shapes are probably caused by the multiple scattering and the lamp's illuminating direction deviation from the 30°, respectively. The peaks work as noises. These noises can be removed by averaging them. The pixel numbers representing the gaps of 5.07 mm, 2.05 mm, and 1.07 mm are 195, 73, and 34, respectively. When 5.07 mm and 195 are set to 1, the gap and the pixel number ratios are given as 1.0:0.40:0.21 and 1.0:0.37:0.17, respectively. The gap and pixel ratios imply that the number of pixels corresponding to smaller gaps decreases more than that predicted by the gap size decreasing ratio. These two ratios are close to each other. But, the difference between them increase ($0.37/0.40 = 0.925$ and $0.17/0.21 = 0.81$) as the gap size becomes

smaller. For the case of Figures 3(d) and 3(e), the shapes do not have a rectangular parallelepiped shape but a wedge, and the intensity differences of the distributions are smaller compared with those in Figures 3(a)–3(c). The number of pixels corresponding to 0.45 mm and 0.17 mm is 7 and 3, respectively. These numbers are much smaller than those predicted by the gap size ratio as expected by the Figures 3(a)–3(c). When the 0.17 mm gap is observed with the microscope of 20 times magnification, the number of pixels given by the Raspberry Pi camera becomes around 240, as shown in Figure 3(f). This number of pixels probably derived because the pixel of the Raspberry Pi camera is $(1.12 \mu\text{m})^2$, while $(4.88 \mu\text{m})^2$ for the Nikon camera. The distribution has the shape of rectangular parallelepiped, though there are many intensity peaks even in dark red color regions.

In the x - y plane of these figures, the 2D pixel intensity distribution is also shown. These 2D intensity distributions are divided into three sections by the colors: two highest intensity sections are represented by dark red color and a lowest intensity section by blue and sky blue. The former represents the top surfaces of the left and right jaws and the latter the top surface of the dark paper in the bottom, i.e., the bottom of the gap. Figure 3 informs that the number of pixels representing the crack width should be as many as possible to estimate the geometrical parameters of the crack. In this regard, the Raspberry Pi camera is good for crack characterization.

Figure 3 allows determining the actual size of the crack in mm with use of equation (1). For the case of Figure 3(f), since the magnified image of the gap 0.17 mm appears at 40 mm distance from the Raspberry Pi camera's objective with the focal length of 3 mm and the image has the size of 3.4 mm by 20 times magnification by the microscope, the number of pixels corresponding to the gap is calculated as 246 by equation (1). This is almost the same as 240 calculated from Figure 3(f). It is also possible to relate the intensity difference $\Delta I = 3.5 \times 10^4$, i.e., $\Delta I = I_{\max} - I_{\min}$, where $I_{\min} = 3.0 \times 10^4$ (bottom of the crack) and $I_{\max} = 6.5 \times 10^4$ (top surface of the crack) in Figure 3(f), to the depth of the gap. Since the jaws' thickness d of the caliper equals to 3.5 mm, $\alpha = d/(I_{\max} - I_{\min}) = d/\Delta I = 1.0 \times 10^{-4}$ mm/gray level (depth resolution).

As mentioned above, the intensity of light from a point radiation source is inversely proportional to the square of the distance. The intensity of the light that illuminates the sample surface will be given as $I_s = I_0/L_s^2$, where I_0 is the illuminating light intensity of a halogen lamp, and I_s and L_s are the light intensity of the lamp at the sample surface and the distance from the lamp to the sample surface, respectively, since the halogen lamp is a point light source. Accordingly, when the crack bottom is illuminated, the distance should be increased by the value of the crack depth. In experimental setup 1, the halogen lamp is located at near the camera to make the distance L_s be nearly the same as the camera distance from the surface L . When light enters into a certain material, a part of the light penetrates into the material and another part is absorbed by the material. Only the part of the entered light that does not penetrate and is not absorbed can be scattered at the surface. The ratio of the part to the entered light is defined

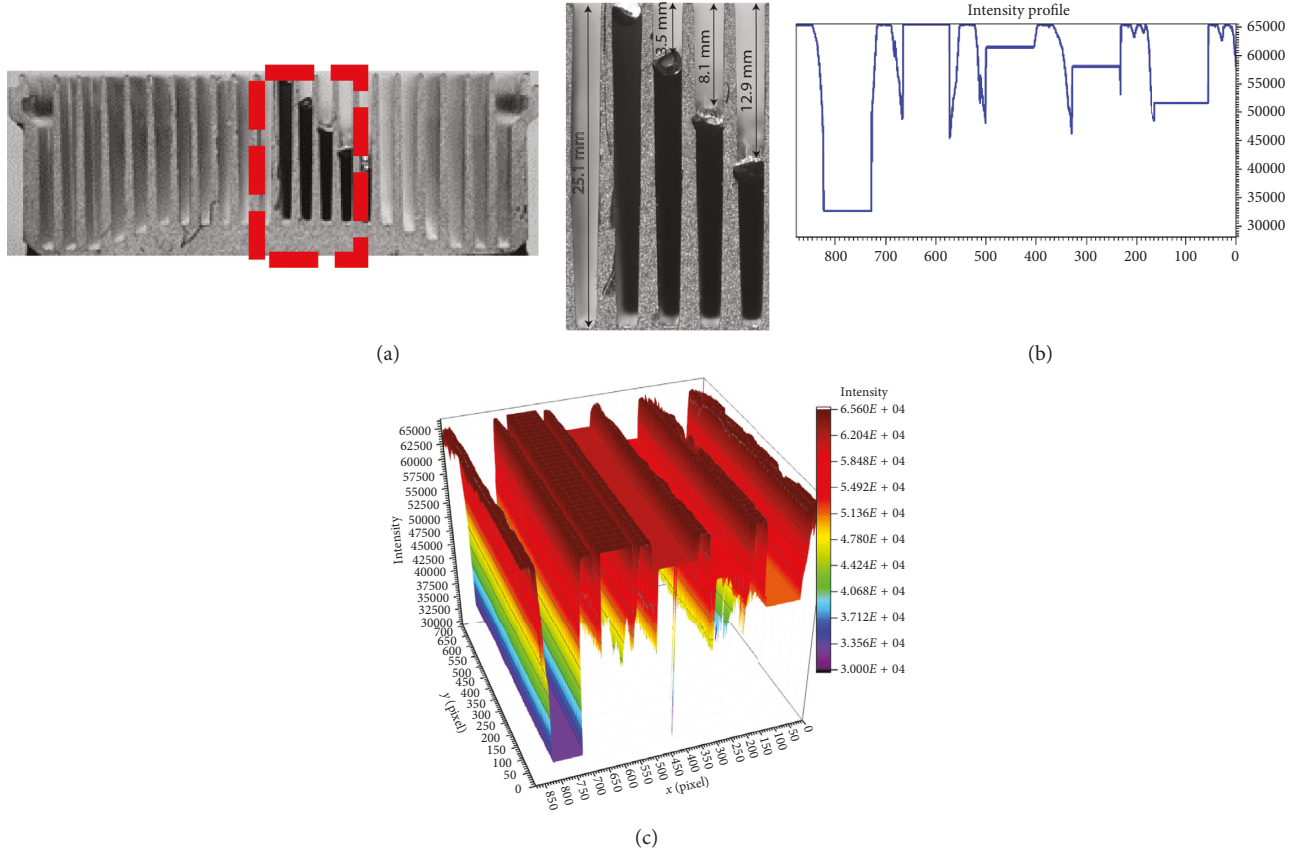


FIGURE 4: A heat dissipater and the pixel intensity distribution: (a) heat dissipater, (b) 2D pixel intensity distribution in averaged gray level, and (c) 3D pixel intensity distribution.

as the surface reflectance γ . When the reflectance of the surface γ_s and that of the crack γ_c are considered, the scattered light intensities at the sample surface and the crack, arriving at the surface of the lens, are expressed as $I_{\text{surface}} = \gamma_s I_s / L^2$ and $I_d = \gamma_c I_s / (L + d)^2$, respectively. With these relationships, the two-intensity ratio $\xi = I_d / I_{\text{surface}}$ will be written as

$$\xi = \frac{I_d}{I_{\text{surface}}} = \frac{\gamma_c}{\gamma_s (1 + (d/L))^2 (1 + (d/L_s))^2}. \quad (2)$$

In equation (2), the lens size effect should also be considered since the light collected by the lens is proportional to lens area. But, in setup 1, when $L \gg d$, the effect can be eliminated, i.e., $\xi = \gamma_c / \gamma_s$. This means that the intensity ratio ξ has no relation with the crack depth d . To avoid this situation, the crack image should be taken with a close-distance photographing or an optical microscope. When the reflectance of the crack and the surface are the same and $L = L_s$, then $\xi \cong 1 / (1 + (d/L))^4$. From this relationship, the crack depth is expressed as

$$d \cong L \left(\frac{1}{\sqrt[4]{\xi}} - 1 \right). \quad (3)$$

The 2nd sample is an aluminum heat dissipater which is composed of multiple blades aligned in parallel with a 2 mm gap between them, as shown in Figure 4(a). Figure 4 shows

the heat dissipater and its pixel intensity distribution. Each blade has the shape of a rectangle, and its one side edge is connected to a common bottom plate, that is, 25.1 mm distance from the top edge of the blades. The top edge thickness of each blade is around 1 mm and the thickness increases as closer to the bottom plate. This dissipater can work as a periodic crack array having the period of 3 mm and the crack depth of 25.1 mm. The period corresponds to around 170 pixels. From this dissipater, only 6 blades specified by a parallelepiped are chosen as the crack sample, and then a piece of aluminum plate with the thickness of about 2 mm is inserted between blades. The inserted depths are no piece, 0 mm, 3.5 mm, 8.1 mm, and 12.9 mm in between blades 1 and 2, 2 and 3, 3 and 4, 4 and 5, and 5 and 6, respectively. So the crack array has a stepwise depth as illustrated by a rectangle in Figure 4(a). When the crack sample is placed at the 1st setup, the averaged pixel intensity distribution in a gray scale, processed by the OriginLab, is shown in Figure 4(b). The distribution reveals the mean gray level of the pixel intensity distribution in 3D form, as shown in Figure 4(c). The gray-level scale image clearly shows stepwise gray level increase of the heat dissipater, though the scale does not match with the original crack object due to 4th order dependence of ξ to distance, as shown in equation (2). For the case of no aluminum piece, the scale has the lowest value. The gray level scale image shows a sharp gray scale

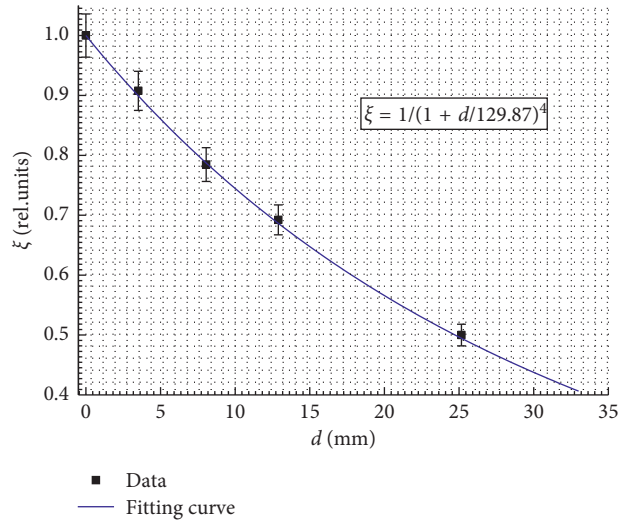


FIGURE 5: Intensity ratio ξ vs. crack depth d and fitting curve $\xi \cong 1/(1 + (d/129.87))^4$.

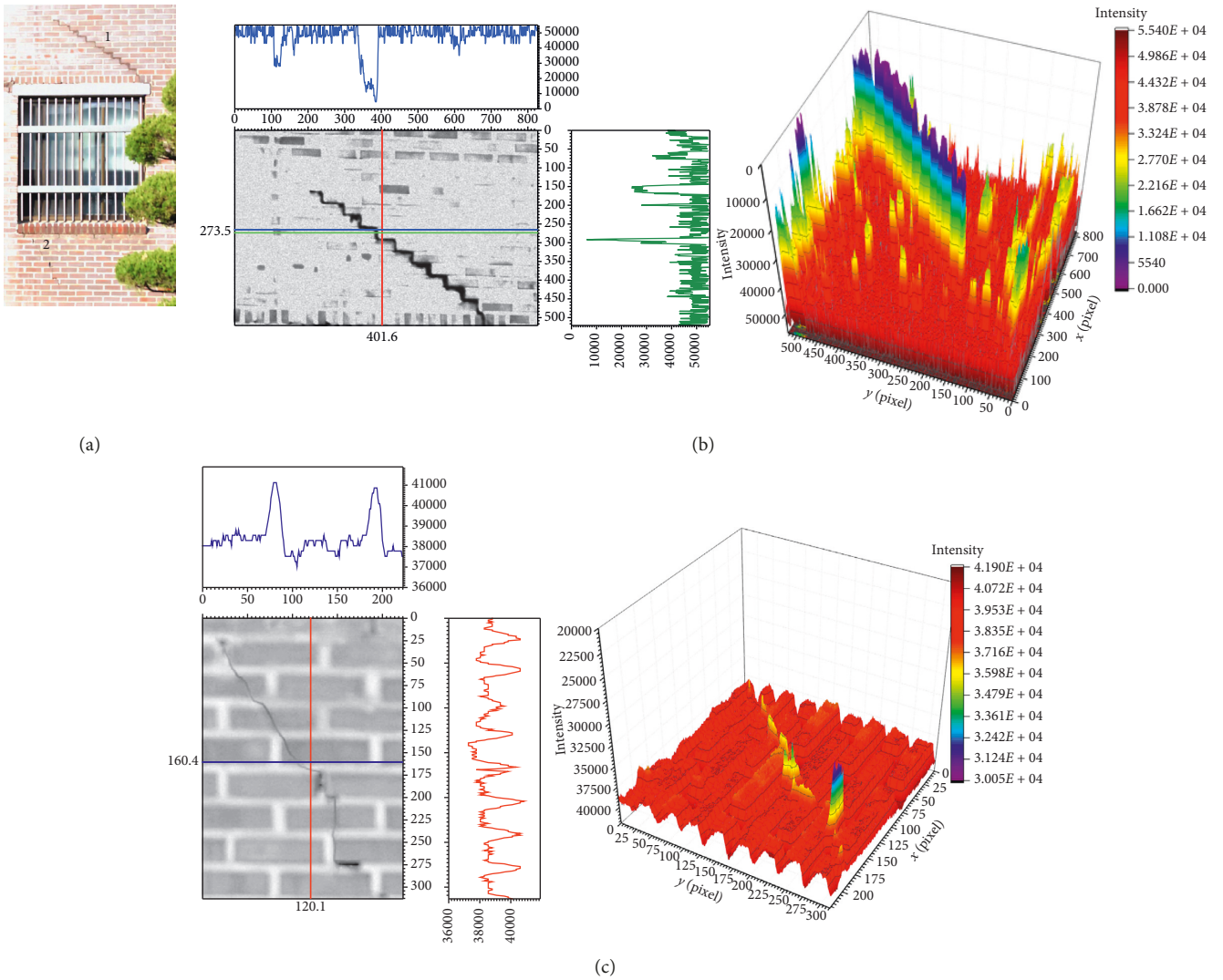
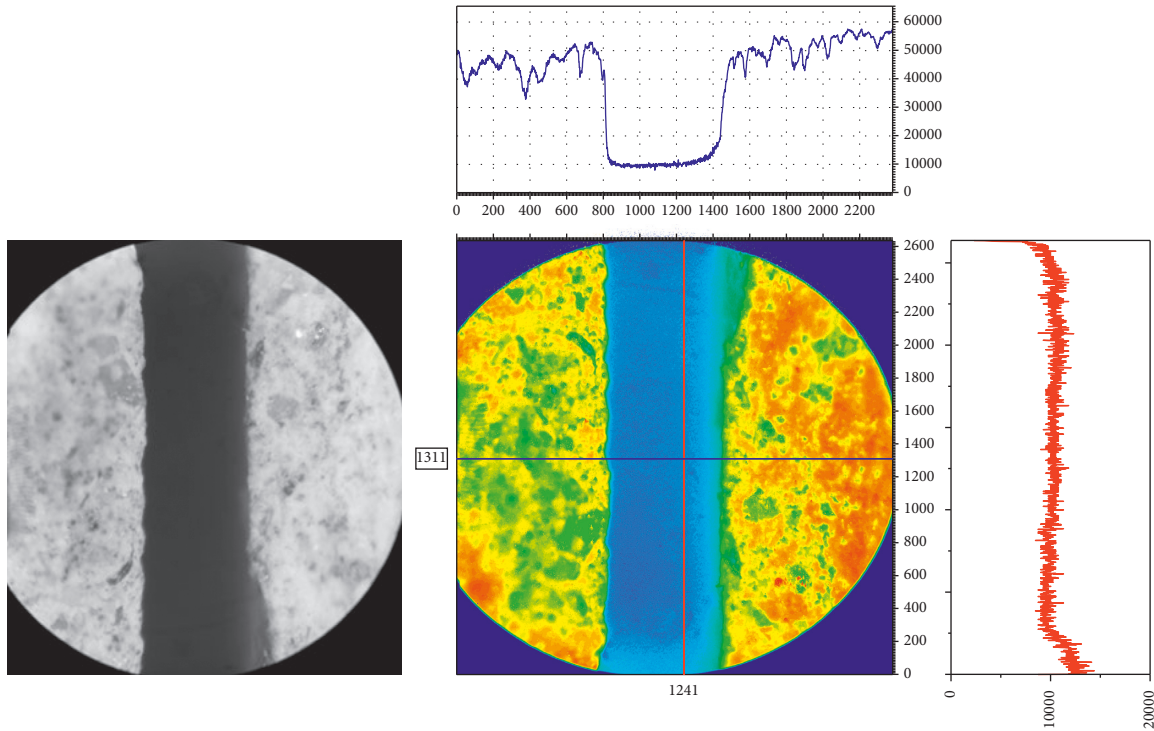
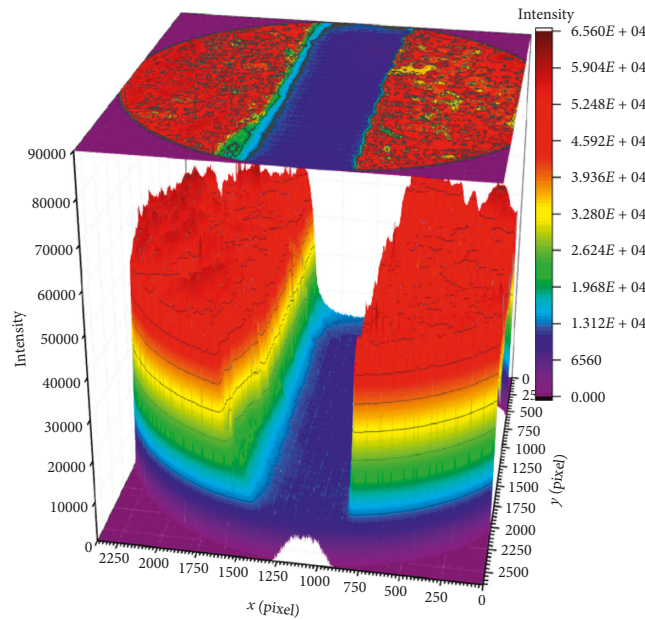


FIGURE 6: Cracks on the wall: (a) a full color image of cracks on the wall of a building, (b) pixel intensity distribution of the crack number 1 in both 2D and 3D forms, and (c) pixel intensity distribution of the crack number 2 in both 2D and 3D forms. The contrast of the crack image is enhanced with use of a hyperspectral filter with the central wavelength of 580 nm.



(a)



(b)

FIGURE 7: Gray scale crack image and its pixel intensity distribution in both 2D and 3D forms.

decrease between the blade and the inserted aluminum piece because the pieces do not have 2 mm thickness. The tips of the blades do not have 1 mm thickness, but smaller.

With the averaged pixel intensity distribution in Figure 4(b), equation (2) allows estimating the crack depth. From equation (2), the expected ξ values for the given d and L values can be calculated when $\gamma_c = \gamma_s$. For the case of the dissipater, γ_c and γ_s are the same because they are the same aluminum. In Figure 5, each ξ value for a given d is

calculated from the mean pixel intensity distribution and is plotted as the data points. The error bar for each data point is given by OriginLab by considering the pixel intensity spread in the crack image. When the data points are fitted, the fitting function is given as $\xi \cong 1/(1 + (d/129.87))^4$. In this function, L is given as 129.87 mm. In experimental setup 1, L is set to $\cong 130$ mm. Two L values are almost the same. This means that the pixel intensity distribution can measure the crack depth with a high accuracy. The error bars indicate that

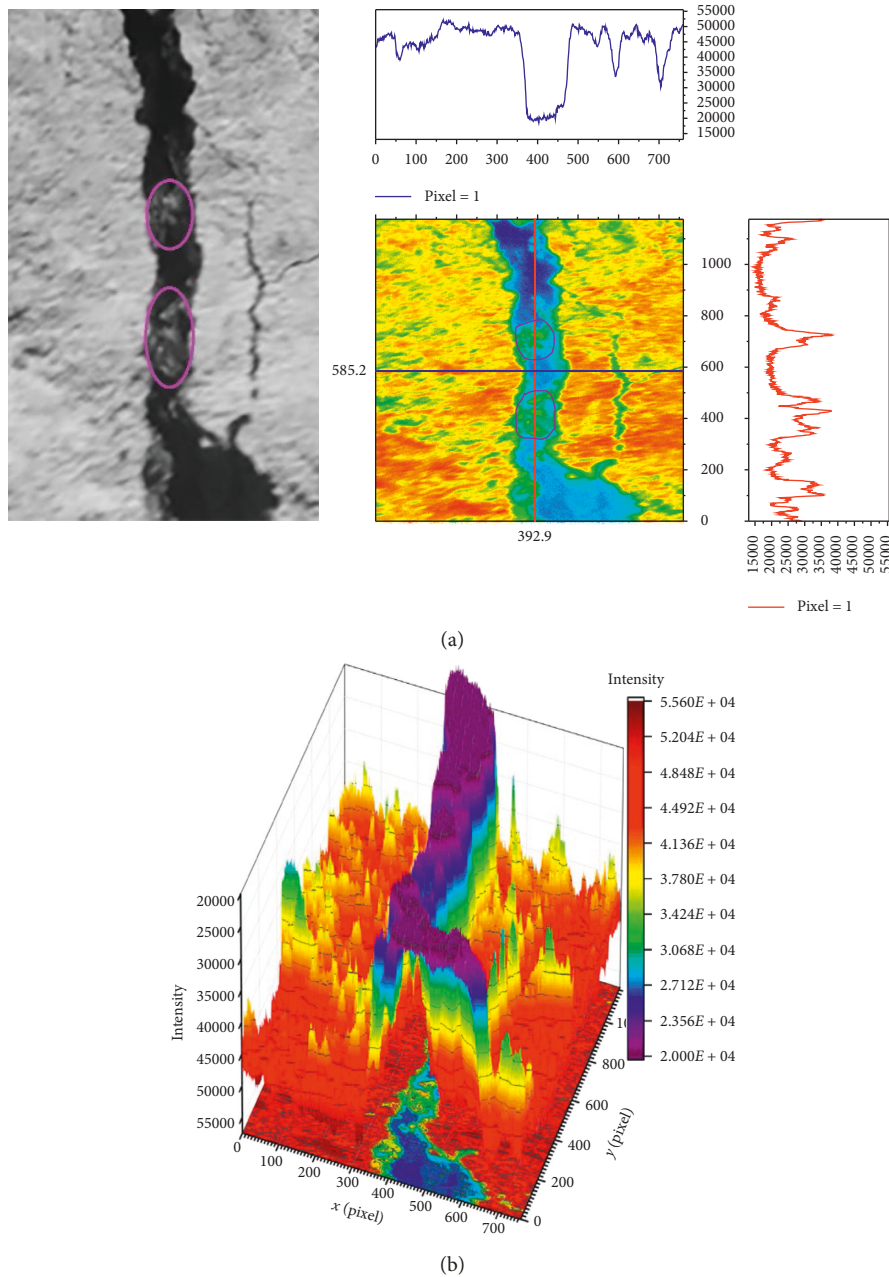


FIGURE 8: Gray scale image of a crack with individual particles and its 2D and 3D intensity distributions.

the depth estimation error increases as the depth becomes smaller. This is because the depth is too small compared with the distance between the crack surface and the lens; the pixel intensity distribution can hardly express the surface and the small depth scattered intensity difference. The expected error from the bars are approximately $\pm 33\%$, $\pm 15\%$, $\pm 10\%$, and $\pm 6\%$ for 3.5 mm, 8.1 mm, 12.9 mm, and 25.1 mm, respectively. Even for the 0 mm case, 1 mm error can be arisen. From the expected errors for different depths, the accuracy of measuring the crack depth can be within $\pm 15\%$.

Figures 3 and 4 clearly state that the pixel intensity distribution can describe the geometrical parameters of the crack, such as width, depth, and shape with a high accuracy.

4. Visualization of the Cracks in Buildings in Three-Dimensional Space

The previous section clearly demonstrates that the pixel intensity distribution can allow calculating the crack depth. This section presents cracks on the wall of a building. The cracks on the wall are practically difficult to access, especially for higher buildings. So, the cracks on the wall can be photographed at a considerable distance.

Figure 6 shows a full color image of cracks on the brick wall of a building, taken at 20 m with the Nikon D810 under the sun illumination with the illumination angle of about 40° above the horizon and the pixel intensity distribution as shown in

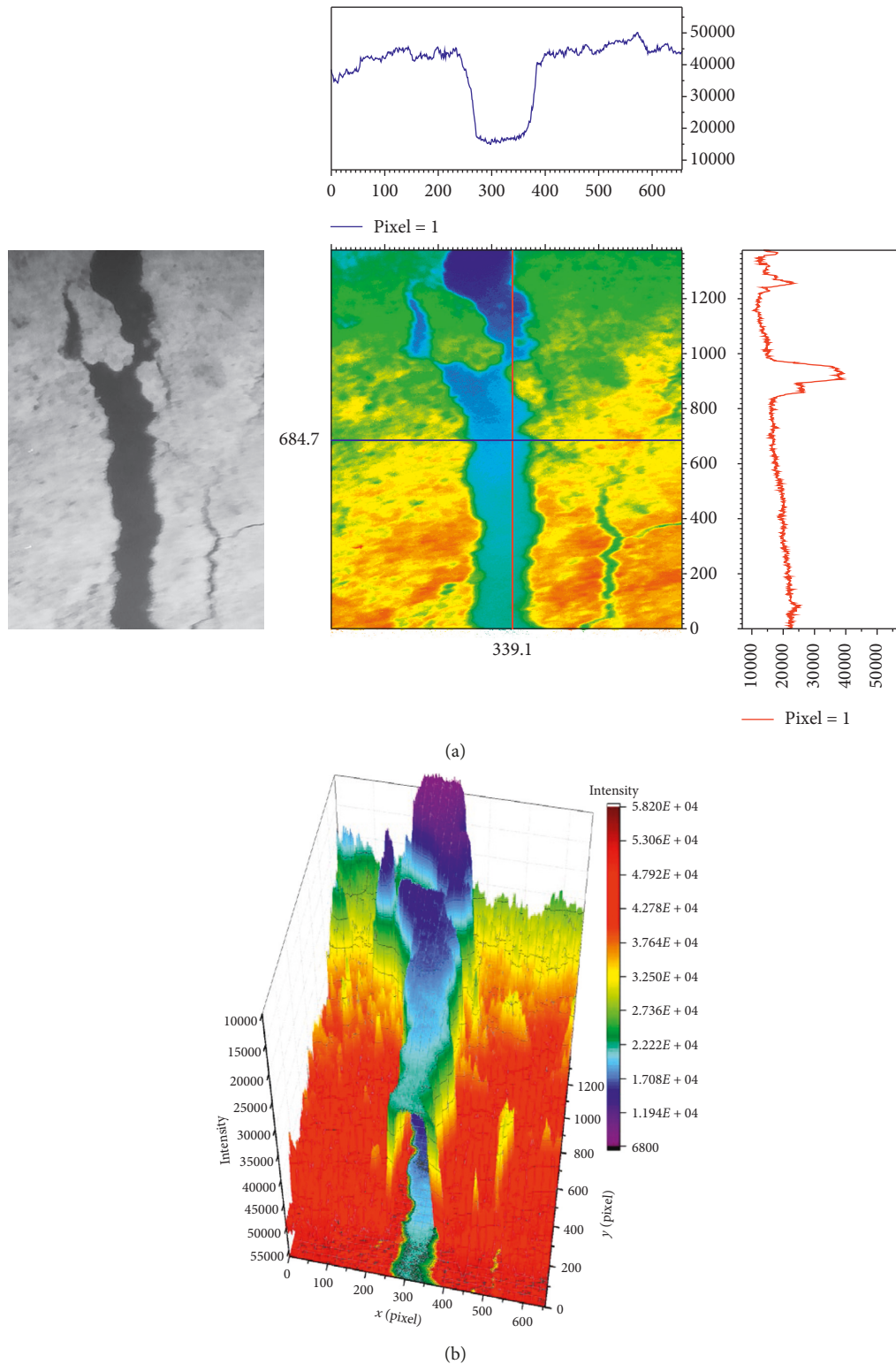
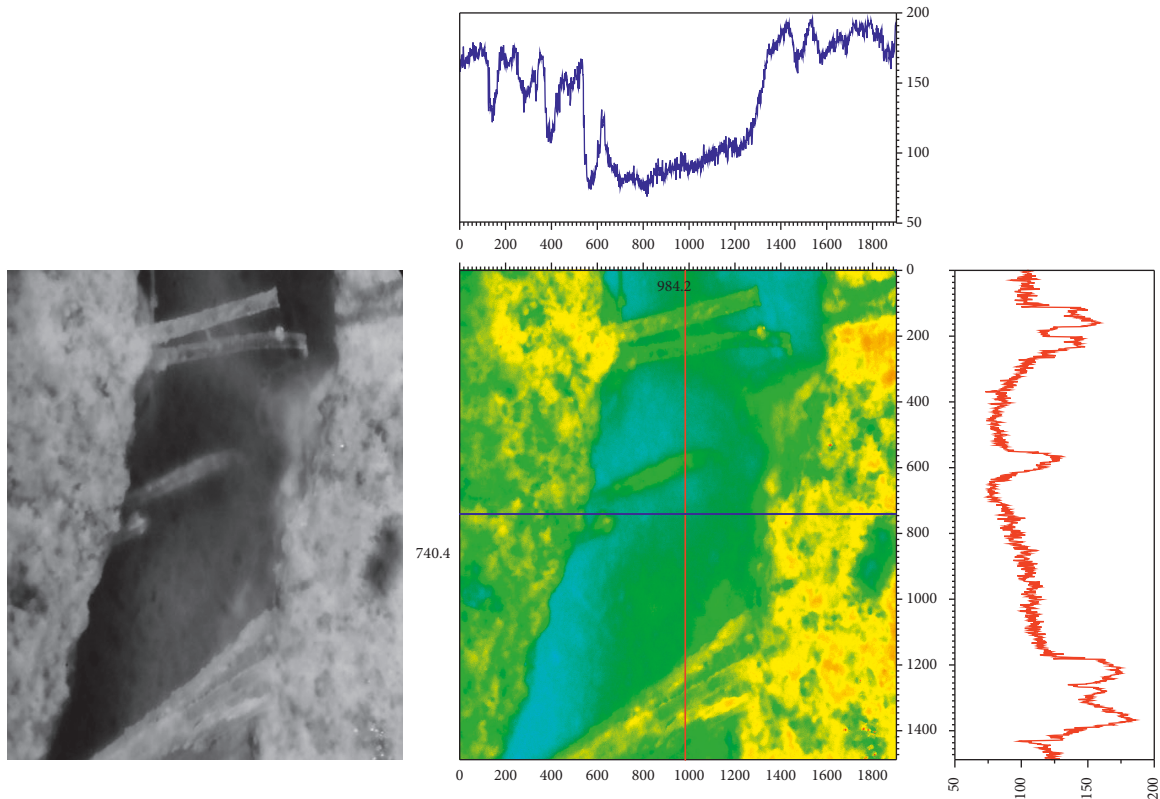


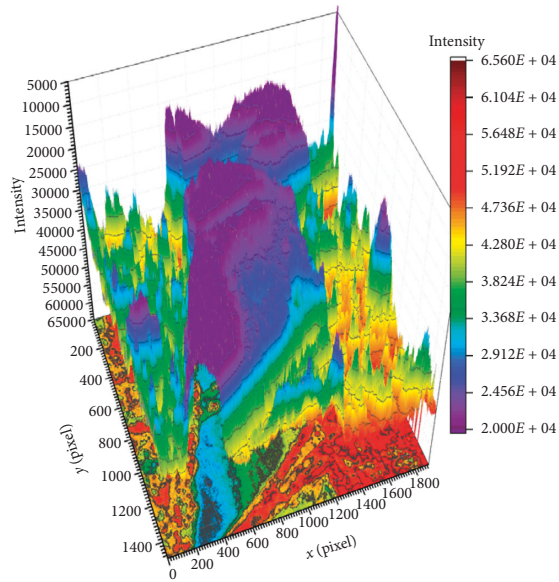
FIGURE 9: Gray scale image of a crack with displaced parts, profiles of reflected light intensity, and 3D graph of crack with the axis of the intensity data.

Figure 4. Two cracks specified with number 1 and 2 are shown. The 2D and 3D form presentations of the distribution still reveal the nonuniform intensity difference though the crack area appears as only darker than its surrounding wall. The

photo was taken on a sunny day, and the angle of inclination of the sun's rays to the surface of the building was approximately 40°. The nonuniform intensity difference implies that the crack has different depths. The crack number 2 is too small to identify



(a)



(b)

FIGURE 10: Gray scale image of a crack with torn filamentous concrete fillers, profiles of reflected light intensity, and 3D graph of crack with the axis of the intensity data.

with the direct photographing, but the crack can still be identified when the photo is taken with a hyperspectral filter centered on the wavelength of 580 nm, as shown in Figure 6(b). The hyperspectral filter can pass the light in the spectral range of 580 ± 5 nm. The intensity distribution in 3D form still reveals the intensity difference.

However, to derive meaningful geometrical parameters of the cracks with the image taken with a camera at a long distance from the cracks, the camera needs to have a detector with a highly sensitive and high resolution with a small pixel to make the crack areas have a large number of pixels, as shown in Figure 3.

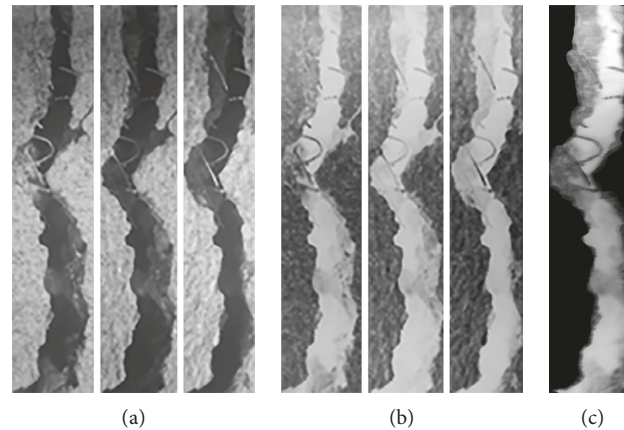


FIGURE 11: Crack images obtained with 3 different illumination angles: (a) three images at different angles of illuminations, (b) gray level inverted image of (a), and (c) the combined image of the three images in (a).

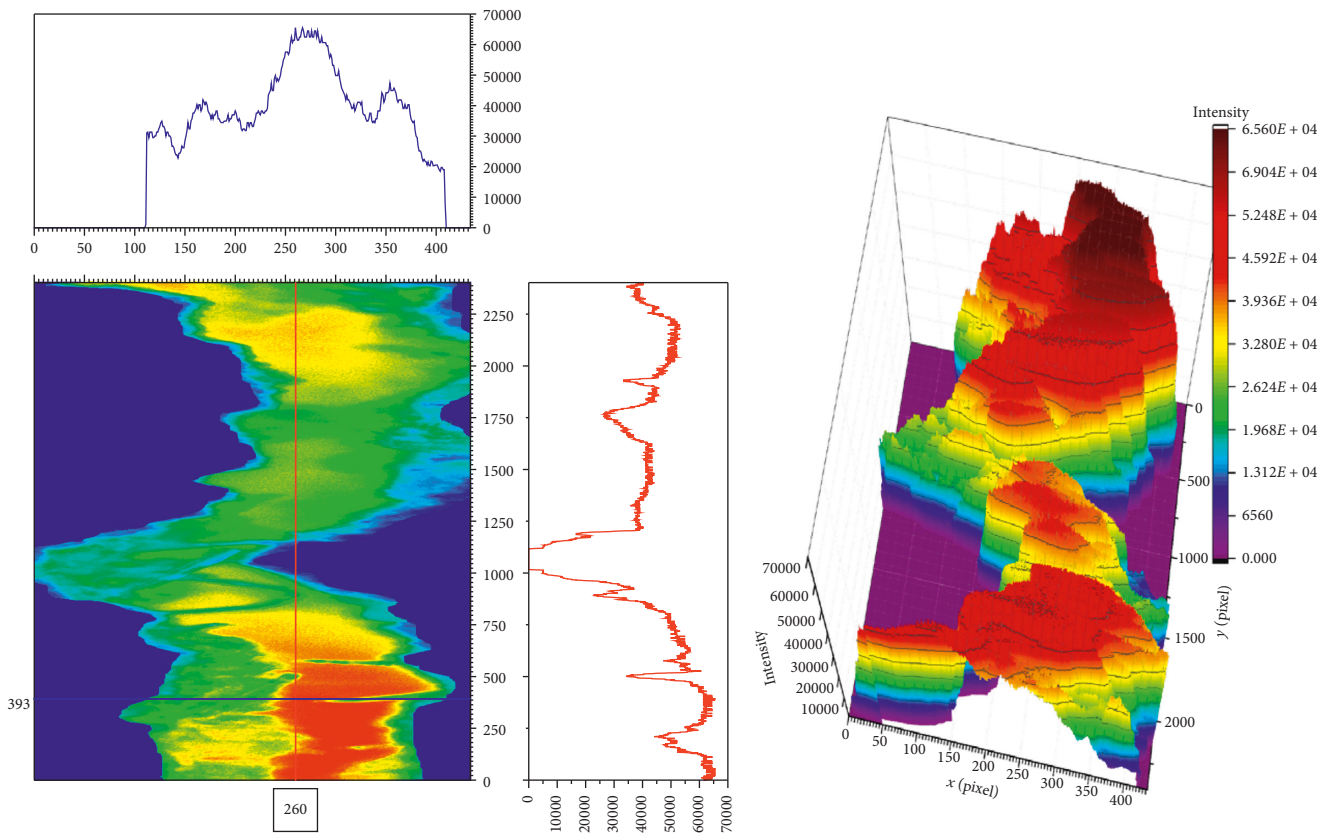


FIGURE 12: Pixel intensity distribution of 2D and 3D forms of the combined image in Figure 11(c).

5. Visualization of Cracks in Concrete in Three-Dimensional Space

Cracks of width smaller than 1 mm are formed in the initial stages of damage to the concrete surface. Hence, detection and characterization of the geometrical parameters of the cracks allow preventing further degradation of the surface. For this purpose, it is necessary to have the crack images with a high spatial resolution, i.e., the number of pixels/mm. One way of getting the high spatial images of cracks is an optical

microscope. In this case, a bright illumination source is necessary to make a small area get more light. Figure 7 shows a gray scale image of a crack obtained with experimental setup 2 and pixel intensity distribution in 2D and 3D forms. The original crack size is around 0.85 mm but it was magnified 25 times by the microscope. Now, the crack image is composed of near 600 pixels across its width. The calculated depth value by equation (3) is in the range from 30.5 mm to 37.4 mm. This value range is closely matched with the measured depth value 35 ± 1 mm with a thin metal

wire and a ruler. The value range is within 87% to 107%. It gives the maximum error of 13%. This error range is comparable with the heat dissipater results.

Measuring the depth of cracks may not always be successful since cracks may be filled with individual particles, small pieces of broken blocks, and exposed reinforcement fibers, as shown in Figures 8–10, respectively. Figure 8 shows a small crack (0.15 mm) with particles. The pixel intensity distribution shows that the particles in the crack are blocking the crack and makes difficult the illuminating light to get into further. The 2D and 3D forms of the intensity distributions clearly show the blocked area by the particle. The areas appear as brighter than other crack gaps. So, this blocked area will present false depth information. This means the crack morphology will be slightly different from the actual morphology. Figures 9 and 10 also show a broken block and fibers appearing within the crack distort the pixel intensity distribution. The effects are not different from the particle case.

6. Computer Synthesis of Images of Complex Cracks

In most cases, the shape of the crack is complex and not straight. In most cases, the shape of the crack is complex and its image becomes different for the different illumination directions. This is shown in Figure 11. In Figure 11, three images of the 0.49 mm crack in a concrete block taken with three different illumination directions are shown in Figure 11(a). The crack widths become different and the presence of many fibers is also shown. The illumination direction changes are simulated by locating the sample on the rotating table (6) in Figure 1(a). The 3 images in Figure 11(a) show the different features and the morphology close to the real shape of the crack. Figure 11(b) shows the gray level inverted images of Figure 11(a). This image shows the crack feature more clearly. When the pixel intensities of these inverted images are added and normalized to combine them as an image, the resulted image is shown in Figure 11(c). The combined image shows all the features of the individual image.

In Figure 12, the pixel intensity distribution in 2D and 3D forms are shown. The distributions will reveal the crack morphology that is close to the real shape of the crack.

7. Conclusion

The pixel intensity distribution of a crack image obtained with close-distance photography or using an optical microscope can be used to measure the geometrical parameters such as width, depth, and morphology of the crack. The 3D form of the distribution reveals the morphology of the crack, the number of pixels between the highest pixel intensity areas, the width of the crack, and the intensity ratio between the highest to that at a specific distance depth of the crack. The accuracy of the estimated parameters obtained with the distribution cannot be exceeded $\pm 10\%$ for the width and $\pm 15\%$ for the depth at the laboratory environment.

The intensity distribution can be applied to real crack environment, if the crack image can be taken with a camera having a highly sensitive detector and a high resolution with a micron range pixel size. It is considered that the accuracy of the crack width and depth estimations will be smaller than the numbers given above if the crack area contains more pixels and the pixel size of the camera is smaller. This will work for the future.

Data Availability

Data used to confirm the results of this study (photographs taken by a NIKON D810 camera with an AF-S Zoom-Nikkor 24–85 mm f/3.5–4.5 G lens with resolution 7360×4912 pixels and an optical microscope with a Raspberry Pi v2 camera with a Sony IMX219 8-megapixel sensor with 3280×2464 pixels' resolution under OmniBS technology) are included in this manuscript.

Conflicts of Interest

The authors declare that they have no conflicts of interest.

Acknowledgments

This work was supported by the Priority Research Centers Program through the National Research Foundation of Korea (NRF) Funded by the Ministry of Education (grant number. NRF-2018R1A6A1 A03025542).

References

- [1] A. Mohan and S. Poobal, "Crack detection using image processing: a critical review and analysis," *Alexandria Engineering Journal*, vol. 57, no. 2, pp. 787–798, 2018.
- [2] C. Koch, K. Georgieva, V. Kasireddy, B. Akinci, and P. Fieguth, "A review on computer vision based defect detection and condition assessment of concrete and asphalt civil infrastructure," *Advanced Engineering Informatics*, vol. 29, no. 2, pp. 196–210, 2015.
- [3] H. Zakeri, F. M. Nejad, and A. Fahimifar, "Image based techniques for crack detection, classification and quantification in asphalt pavement: a review," *Archives of Computational Methods in Engineering*, vol. 24, no. 4, pp. 935–977, 2016.
- [4] T. Dawood, Z. Zhu, and T. Zayed, "Machine vision-based model for spalling detection and quantification in subway networks," *Automation in Construction*, vol. 81, pp. 149–160, 2017.
- [5] H. Son, C. Kim, and C. Kim, "Automated color model-based concrete detection in construction-site images by using machine learning algorithms," *Journal of Computing in Civil Engineering*, vol. 26, no. 3, pp. 421–433, 2012.
- [6] B. Y. Lee, Y. Y. Kim, S.-T. Yi, and J.-K. Kim, "Automated image processing technique for detecting and analysing concrete surface cracks," *Structure and Infrastructure Engineering*, vol. 9, no. 6, pp. 567–577, 2013.
- [7] H.-N. Nguyen, T.-Y. Kam, and P.-Y. Cheng, "An automatic approach for accurate edge detection of concrete crack utilizing 2D geometric features of crack," *Journal of Signal Processing Systems*, vol. 77, no. 3, pp. 221–240, 2014.

- [8] X. W. Ye, C. Z. Dong, and T. A. Liu, "Review of machine vision-based structural health monitoring: methodologies and applications," *Journal of Sensors*, vol. 2016, Article ID 7103039, 10 pages, 2016.
- [9] H. Kim, J. Lee, E. Ahn, S. Cho, M. Shin, and S.-H. Sim, "Concrete crack identification using a UAV incorporating hybrid image processing," *Sensors*, vol. 17, no. 9, p. 2052, 2017.
- [10] J.-H. Chen, M.-C. Su, R. Cao, S.-C. Hsu, and J.-C. Lu, "A self organizing map optimization based image recognition and processing model for bridge crack inspection," *Automation in Construction*, vol. 73, pp. 58–66, 2017.
- [11] R. S. Adhikari, O. Moselhi, and A. Bagchi, "Image-based retrieval of concrete crack properties for bridge inspection," *Automation in Construction*, vol. 39, pp. 180–194, 2014.
- [12] L. Wu, S. Mokhtari, A. Nazeif, B. Nam, and H.-B. Yun, "Improvement of crack-detection accuracy using a novel crack defragmentation technique in image-based road assessment," *Journal of Computing in Civil Engineering*, vol. 30, no. 1, Article ID 04014118, 2014.
- [13] P. Prasanna, K. J. Dana, N. Gucunski et al., "Automated crack detection on concrete bridges," *IEEE Transactions on Automation Science and Engineering*, vol. 13, no. 2, pp. 591–599, 2014.
- [14] T. Yamaguchi and S. Hashimoto, "Fast crack detection method for large-size concrete surface images using percolation based image processing," *Machine Vision Application*, vol. 21, no. 5, pp. 787–809, 2010.
- [15] Q. Zou, Y. Cao, Q. Li, Q. Mao, and S. Wang, "CrackTree: automatic crack detection from pavement images," *Pattern Recognition Letters*, vol. 33, no. 3, pp. 227–238, 2012.
- [16] N.-D. Hoang, "Detection of surface crack in building structures using image processing technique with an improved Otsu method for image thresholding," *Advances in Civil Engineering*, vol. 2018, Article ID 3924120, 10 pages, 2018.
- [17] Y.-S. Yang, C.-L. Wu, T. T. C. Hsu, H.-C. Yang, H.-J. Lu, and C.-C. Chang, "Image analysis method for crack distribution and width estimation for reinforced concrete structures," *Automation in Construction*, vol. 91, pp. 120–132, 2018.
- [18] L. L. Jeune, S. Robert, E. L. Villaverde, and P. Claire, "Plane wave imaging for ultrasonic non-destructive testing: generalization to multimodal imaging," *Ultrasonics*, vol. 64, pp. 128–138, 2016.
- [19] Ultrasonic Concrete Testing Equipment, <https://www.pcte.com.au/pundit-pl-200-ultrasonic-pulse-velocity>.
- [20] Ultrasonic Testing Product, <https://www.canopusinstruments.com>.
- [21] S. A. Shevchik, B. Meylan, G. Violakis, and K. Wasmer, "3D reconstruction of cracks propagation in mechanical workpieces analyzing non-stationary acoustic mixtures," *Mechanical Systems and Signal Processing*, vol. 119, pp. 55–64, 2019.
- [22] H. S. Eddine, R. M. Pitti, E. Badel, and G. Joseph, "Reconstruction of the 3D crack profile in wood based structures by X-ray computed microtomography," in *Proceedings of the JET 2018*, vol. 6, Marrakech, Morocco, May 2018.
- [23] C. Cai, T. Bore, F. Delaine, N. Gasnier, and E. Vourc'h, "3D reconstruction of surface cracks using bi-frequency eddy current images and a direct semi-analytic model," *Journal of Physics: Conference Series*, vol. 904, Article ID 012019, 2017.
- [24] Y.-F. Liu, S. Cho, B. F. Spencer, and J.-S. Fan, "Concrete crack assessment using digital image processing and 3D scene reconstruction," *Journal of Computing in Civil Engineering*, vol. 30, no. 1, Article ID 04014124, 2016.
- [25] Z. Ma and S. Liu, "A review of 3D reconstruction techniques in civil engineering and their applications," *Advanced Engineering Informatics*, vol. 37, pp. 163–174, 2018.
- [26] M. R. Jahanshahi and S. Masri, "Image-based crack quantification," US Patent US009235902B2, University of Southern California (USC), Pasadena, CA, USA, 2016.
- [27] B. Shan, S. Zheng, and J. Ou, "A stereovision-based crack width detection approach for concrete surface assessment," *KSCE Journal of Civil Engineering*, vol. 20, no. 2, pp. 803–812, 2016.
- [28] S. Cho, S. Park, G. Cha, and T. Oh, "Development of image processing for crack detection on concrete structures through terrestrial laser scanning associated with the octree structure," *Applied Sciences*, vol. 8, no. 12, 2018.
- [29] G. Li, S. He, Y. Ju, and K. Du, "Long-distance precision inspection method for bridge cracks with image processing," *Automation in Construction*, vol. 41, pp. 83–95, 2014.
- [30] OriginLab, Image Processing, <https://www.originlab.com/index.aspx?go=Products/Origin/DataAnalysis/ImageProcessing>.
- [31] J.-Y. Jung, H.-J. Yoon, and H.-W. Cho, "A study on crack depth measurement in steel structures using image-based intensity differences," *Advances in Civil Engineering*, vol. 2018, Article ID 7530943, 10 pages, 2018.
- [32] Nikon Corporation USA, *Digital Camera Nikon D810, User's Manual*, Nikon Corporation USA, Melville, NY, USA, <https://www.nikon-usa.com/en/nikon-products/product/dslr-cameras/d810.html>.
- [33] Raspberry Pi Camera Module V2 - 8 Megapixel, 1080p. <https://www.argon40.com/raspberry-pi-camera-module-v2.html>; <https://www.raspberrypi.org/products/camera-module-v2/>.
- [34] A T10 Illuminance Meter from Konica Minolta Sensing Inc. <https://sensing.konicaminolta.asia/wp-content/uploads/2017/08/T-10-and-T-10M-Illuminance-Meters.pdf>.
- [35] G. Woan, *The Cambridge Handbook of Physics Formulas*, Cambridge University Press, Cambridge, UK, 2003, <http://www.cambridge.org/9780521573498>.
- [36] A. Jacobs, *SynthLight Handbook, Chapter 1: Fundamentals, the Inverse Square Law*, London Metropolitan University, London, UK, 2004, <http://www.learn.londonmet.ac.uk/packages/synthlight/index.html>.
- [37] Mitutoyo 500-195-30CAL Absolute Digimatic Caliper with Calibration, Stainless Steel Jaws, 0–4 Range, 0.0005 Resolution, –0.001 Accuracy, <https://www.mitutoyo.co.jp/eng/products/nogisu/hyojyun.html>.

